Supporting information for verified Sun–Jupiter Hill region topology and parameter sensitivity

Supplementary Note S1: Equilibrium quintics, the global minimum, and Hill-region classification

This note supplies classical mathematical details used in the manuscript. The equations and equilibrium theory belong to the standard circular restricted three-body problem[1]. The Jensen argument below is included as a self-contained exposition; no claim of historical priority or a new minimum theorem is made. The new, parameter-specific computation is the interval certificate described in the manuscript and Supplementary Note S2.

S1.1 Definitions and the five equilibria

Let $0 < \mu < 1/2$, place the two primaries at $(-\mu,0)$ and $(1-\mu,0)$, and define

$$r_1^2 = (x+\mu)^2 + y^2, r_2^2 = (x-1+\mu)^2 + y^2. \quad (1)$$

$$U = 2\Omega = x^2 + y^2 + \frac{2(1-\mu)}{r_1} + \frac{2\mu}{r_2}. \quad (2)$$

The domain excludes the two collision points. The unshifted Jacobi constant is $C = U - v_x^2 - v_y^2$. An equilibrium has zero rotating velocity and satisfies $\nabla\Omega=0$. On $y=0$, write $F=\Omega_x$. Direct differentiation on each collision-free interval gives

$$F_x = 1 + \frac{2(1-\mu)}{|x+\mu|^3} + \frac{2\mu}{|x-1+\mu|^3} > 0. \quad (3)$$

On $(-\infty,-\mu)$, F tends to $-\infty$ at the left end and $+\infty$ at the right end. On $(-\mu,1-\mu)$, its one-sided limits are $-\infty$ and $+\infty$. On $(1-\mu,\infty)$, the same limiting signs hold. Continuity and strict monotonicity therefore give exactly one root in each interval, labeled L3, L1, and L2 respectively. This proof does not depend on numerical starting guesses.

For $y\neq0$, $\Omega_y=0$ implies $(1-\mu)/r_1^3+\mu/r_2^3=1$. Substitution into $\Omega_x=0$ then gives

$$\mu(1-\mu)\left(\frac{1}{r_2^3} - \frac{1}{r_1^3}\right) = 0. \quad (4)$$

Consequently $r_1=r_2=1$. The only noncollinear equilibria are L4 and L5, with coordinates $(1/2-\mu,\pm\sqrt{3}/2)$. Thus there are exactly five equilibria in the stated model.

S1.2 Interval-specific collinear quintics

The distance variable γ is positive and is defined separately on each physical interval. Denominators must be cleared only after fixing those intervals; otherwise signs of absolute values may be lost. The equations below give polynomials equivalent to the equilibrium equation on their stated domains, not formulas for arbitrary roots of the quintics.

For L1, put $x=1-\mu-\gamma$ with $0<\gamma<1$. Then $r_1=1-\gamma$ and $r_2=\gamma$, so

$$F = 1 - \mu - \gamma - \frac{1-\mu}{(1-\gamma)^2} + \frac{\mu}{\gamma^2}. \quad (5)$$

Multiplication by $-\gamma^2(1-\gamma)^2$ gives the L1 quintic:

$$P_1(\gamma) = \gamma^5 - (3-\mu)\gamma^4 + (3-2\mu)\gamma^3 - \mu\gamma^2 + 2\mu\gamma - \mu = 0. \quad (6)$$

For L2, put $x=1-\mu+\gamma$ with $\gamma>0$. Then $r_1=1+\gamma$ and $r_2=\gamma$, and

$$F = 1 - \mu + \gamma - \frac{1-\mu}{(1+\gamma)^2} - \frac{\mu}{\gamma^2}. \quad (7)$$

Multiplication by $\gamma^2(1+\gamma)^2$ gives

$$P_2(\gamma) = \gamma^5 + (3-\mu)\gamma^4 + (3-2\mu)\gamma^3 - \mu\gamma^2 - 2\mu\gamma - \mu = 0. \quad (8)$$

For L3, γ is the distance from the primary at x=−μ: put x=−μ−γ with γ>0. Then $r_1=\gamma$ and $r_2=1+\gamma$, and

$$F = -\mu - \gamma + \frac{1-\mu}{\gamma^2} + \frac{\mu}{(1+\gamma)^2}. \quad (9)$$

Multiplication by $-\gamma^2(1+\gamma)^2$ gives

$$P_3(\gamma) = \gamma^5 + (2+\mu)\gamma^4 + (1+2\mu)\gamma^3 - (1-\mu)\gamma^2 - 2(1-\mu)\gamma - (1-\mu) = 0. \quad (10)$$

None of the multipliers vanishes on its physical domain. Each quintic therefore has exactly one root in the stated domain, by the uniqueness argument for F. Roots outside that domain must not be assigned to that equilibrium by the same coordinate formula. In particular, the L3 distance is measured from the Sun-side primary, whereas the L1 and L2 distances are measured from the secondary.

As an algebra check, expanding the three denominator-clearing identities with exact rational polynomial coefficients gives $P_1=-\gamma^2(1-\gamma)^2F$, $P_2=\gamma^2(1+\gamma)^2F$, and $P_3=-\gamma^2(1+\gamma)^2F$ identically. Substituting the 18 high-precision collinear benchmark roots from the six recorded input sets gives a maximum absolute quintic residual below 4.75×10^{-89}. Both checks are reproduced by analysis/quintic_algebra_check.py, with machine-readable results in results/quintic_algebra_checks.json. This residual is a calculation check at the printed benchmark roots, not a physical error estimate or the basis of the interval proof. The sixth input set is the DE440 kernel serialization check, not a sixth distinct historical parameterization.

S1.3 Global minimum by a weighted convexity argument

Set p=1−μ, q=μ, and

$$A = pr_1^2 + qr_2^2 = x^2 + y^2 + \mu(1-\mu) > 0. \quad (11)$$

The function $h(s)=1/\sqrt{s}$ is strictly convex for s>0:

$$h''(s) = \frac{3}{4s^{5/2}} > 0. \quad (12)$$

Jensen's inequality therefore gives $p/r_1+q/r_2 \geq 1/\sqrt{A}$. It follows that

$$U = A - \mu(1-\mu) + 2\left(\frac{p}{r_1} + \frac{q}{r_2}\right) \geq A + \frac{2}{\sqrt{A}} - \mu(1-\mu) \geq 3 - \mu(1-\mu). \quad (13)$$

The last scalar inequality follows because $g(A)=A+2/\sqrt{A}$ has derivative $1-1/(A\sqrt{A})$, so its unique global minimum is g(1)=3. Equality in Jensen requires $r_1^2=r_2^2$; equality in the last step requires A=1. Together these give $r_1=r_2=1$, attained only at L4 and L5. Thus U has exactly these two global minima, and $C_4=C_5=3-\mu(1-\mu)$. Adding μ(1−μ) to U and C shifts both minima to the value 3 without changing the equations of motion or any permitted region.

S1.4 Critical topology and the meaning of an open neck

For a fixed Jacobi constant, the Hill region is $H_C=\{q:U(q)\geq C\}$, excluding collisions; U(q)<C is forbidden because it would require negative squared speed. The zero-velocity locus U=C is a configuration-space energetic boundary. It is not generally a phase-space separatrix or a guarantee that any selected orbit will transit an opening.

For the certified historical envelope, $C_1>C_2>C_3>C_4=C_5$. The collinear points are nondegenerate saddles of U, and the triangular points are minima. Since U diverges at both collisions and at infinity, a sufficiently high superlevel set has separate allowed neighborhoods of each primary and an exterior allowed component. There are no further critical points at which this pattern could change. The standard saddle transitions produce the following regimes[1]:

$C>C_1$: The two primary neighborhoods and the exterior are disconnected.

$C_2<C<C_1$: The two primary neighborhoods connect through L1; the exterior remains separate.

$C_3<C<C_2$: The L2 passage connects the interior to the exterior; the L3 passage remains closed.

$C_4<C<C_3$: All three collinear passages have opened; two forbidden islands remain around L4 and L5.

$C=C_4$: There is no forbidden open region; U=C consists of the two triangular points.

$C<C_4$: All collision-free positions are energetically allowed and U=C is empty.

At $C=C_1,C_2,C_3$ the corresponding neck has zero width. Its equilibrium point is an energetic contact, not a finite-width transit passage: an orbit that reaches an equilibrium with zero velocity at finite time must be the equilibrium solution by uniqueness of the smooth local equations. The manuscript therefore illustrates noncritical levels on either side of the transitions. At $C=C_4$, the two zero-velocity points are a degenerate level set; they do not bound a forbidden open region. The raster figures illustrate this analytic classification rather than establish it by pixel connectivity.

S1.5 Planar spectral classification

The position variations satisfy $d(\delta x)/dt=\delta v_x$ and $d(\delta y)/dt=\delta v_\gamma$. Linearizing the accelerations gives

$$\frac{d\delta v_x}{dt} = \Omega_{xx}\delta x + \Omega_{xy}\delta y + 2\delta v_y, \tag{14}$$

$$\frac{d\delta v_y}{dt} = \Omega_{xy}\delta x + \Omega_{yy}\delta y - 2\delta v_x. \tag{15}$$

with characteristic polynomial

$$\lambda^4 + (4 - \Omega_{xx} - \Omega_{yy})\lambda^2 + \Omega_{xx}\Omega_{yy} - \Omega_{xy}^2. \tag{16}$$

At every collinear point, $\Omega_{x\gamma}=0$ and $\Omega_{xx}=F_x>0$. The certificate verifies $\Omega_{\gamma\gamma}<0$ uniformly on all three collinear branches throughout the historical envelope. The constant coefficient is therefore negative. As a quadratic in λ^2, the polynomial has two real roots of opposite signs; hence the spectrum contains one real pair and one imaginary pair. Each collinear equilibrium is of saddle–center type and is linearly unstable in the plane.

At L4 and L5, the characteristic polynomial reduces to $\lambda^4+\lambda^2+27\mu(1-\mu)/4$. If $0<27\mu(1-\mu)<1$, its two λ^2 roots are distinct and negative, giving two purely imaginary eigenvalue pairs. The corresponding positive frequencies are those in Equation (7) of the manuscript. The certificate verifies that condition over the complete historical envelope. This spectral statement alone is not a proof of nonlinear stability; the separately cited planar nonlinear theorem and its exclusions are discussed in the manuscript.

Reversing both Coriolis signs leaves this even characteristic polynomial unchanged. Consequently, frequency agreement or Jacobi conservation alone cannot determine the rotation convention. The sign-sensitive inertial-acceleration and phase comparisons in Supplementary Note S3 address that separate implementation question.

Supplementary Note S2 Source provenance and the uniform certificate

Published inputs and what was compared

The five historical parameterizations are not five independent estimates with a common statistical error model. The first two are rounded constants used in restricted three-body papers; the other three are ratios from JPL ephemeris inputs. The interval connecting them is an explicitly selected historical model envelope. Treating each published decimal string as an exact

input defines a mathematical comparison, not a claim that the physical masses are exactly known.

Koon and colleagues use $\mu = 0.0009537$ in their Sun–Jupiter model, as do Wilczak and Zgliczyński[2,3]. Koon's original paper, page 431, includes $\mu(1-\mu)/2$ in its potential; its C convention is therefore our shifted C_s. Those quoted parameters do not separately document whether satellite masses are included. We preserve that uncertainty in the secondary definition. We do not label them as planet-only measurements.

Efthymiopoulos[4] gives $\mu = 0.00095387536$ explicitly on page 196. The publisher assigns the proceedings issue to 2004 and reports online publication in 2005; the bibliography uses the issue year. This value is not a rounding of the adopted DE440 ratio. Its original heliocentric Hamiltonian presentation is not a table in the same barycentric coordinates used here; the current comparison recomputes coordinates from its quoted μ rather than copying unlike coordinate systems.

The DE405 ASCII header[5] maps names in GROUP 1040 to numbers in GROUP 1041. Its GMS and GM5 entries are $0.295912208285591095 \times 10^{-3}$ and $0.282534590952422643 \times 10^{-6}$ au^3 day^{-2}. Their units cancel in μ. The upper envelope endpoint is exactly

$$\mu_{max} = \frac{282534590952422643}{296194742876543517643}. \tag{17}$$

The DE431 kernel[6] gives BODY10_GM = $1.3271244004193938 \times 10^{11}$ and BODY5_GM = $1.2671276480000021 \times 10^{8}$ km^3 s^{-2}. The DE440 SSD table gives the adopted strings 132712440041.279419 and 126712764.100000 in the same units[7]. BODY5 represents the Jovian system; it must not be confused with planet-only BODY599. The DE440 kernel[8] gives slightly different terminal decimal serialization, $1.3271244004127942 \times 10^{11}$ and $1.2671276409999998 \times 10^{8}$. This sixth recorded input is a serialization cross-check, not an additional historical parameterization. Its effect is negligible at the manuscript's printed precision.

Complete common-convention benchmark

Table S1 reports recomputed collinear coordinates and both Jacobi conventions at the five historical inputs. In every collinear row y=0. L4 and L5 have the same $x=1/2-\mu$ and opposite $y=\pm\sqrt{3}/2$. Their coordinates in Table S2 are analytic; no nonlinear solver is used to define them. C is the unshifted convention of manuscript Equation (1), and $C_s = C+\mu(1-\mu)$. Additional digits are retained in the CSV solely to reproduce the exact specified model. All table quantities are dimensionless.

Table S1 | Recomputed collinear equilibria. All columns are dimensionless; y=0. Efthym. denotes Efthymiopoulos. Exact input strings and higher-precision values accompany the archive.

Input	Point	x	C	C_s
Koon / Wilczak	L1	0.932369752416	3.038756279689	3.039709070145
Koon / Wilczak	L2	1.068826326563	3.037484426527	3.038437216983
Koon / Wilczak	L3	-1.000397374953	3.000953680879	3.001906471335
Efthym.	L1	0.932365587292	3.038760836776	3.039713802258
Efthym.	L2	1.068830521186	3.037488749748	3.038441715230
Efthym.	L3	-1.000397448019	3.000953856232	3.001906821714
DE405	L1	0.932365449056	3.038760988024	3.039713959315

Input	Point	x	C	C_s
DE405	L2	1.068830660400	3.037488893234	3.038441864525
DE405	L3	-1.000397450445	3.000953862052	3.001906833343
DE431	L1	0.932365449606	3.038760987422	3.039713958690
DE431	L2	1.068830659846	3.037488892663	3.038441863931
DE431	L3	-1.000397450435	3.000953862029	3.001906833297
DE440	L1	0.932365449731	3.038760987286	3.039713958548
DE440	L2	1.068830659720	3.037488892533	3.038441863796
DE440	L3	-1.000397450433	3.000953862024	3.001906833286

Table S2 | Analytic triangular equilibria. For each row y=±√3/2; L4 uses the positive sign and L5 the negative sign. All columns are dimensionless.

Input	$x_4 = x_5$	$C_4 = C_5$	$C_{s4} = C_{s5}$
Koon / Wilczak	0.499046300000	2.999047209544	3 (exact)
Efthym.	0.499046124640	2.999047034518	3 (exact)
DE405	0.499046118820	2.999047028709	3 (exact)
DE431	0.499046118843	2.999047028732	3 (exact)
DE440	0.499046118848	2.999047028737	3 (exact)

Outward rounding and the proof conditions

The program represents an interval by two Decimal endpoints. Addition and multiplication evaluate endpoint combinations using ROUND_FLOOR for lower bounds and ROUND_CEILING for upper bounds. Reciprocals use [1/b,1/a] when zero is excluded from [a,b]; division combines multiplication and a reciprocal. Integer powers use repeated interval multiplication, and sign reversal uses exact endpoint negation. No binary float supplies any certificate endpoint, mass ratio, or sign decision. A separate Fraction interval implementation evaluates the same rational formulas exactly and verifies containment inside the Decimal results.

For each of 256 closed parameter panels M, the script first constructs candidate root boxes and then checks $F(a,M)<0<F(b,M)$ as strict interval inequalities. Each box stays inside its physical collision-free branch. Positivity of F_x proves uniqueness; opposite signs and continuity prove existence for every μ in M. The coverage checks include both envelope endpoints. The rational implementation re-evaluates the endpoint signs, root-box functions, and derived bounds; it does not merely compare rounded decimal strings.

For fixed signs $s_1=\mathrm{sign}(x+\mu)$ and $s_2=\mathrm{sign}(x-1+\mu)$, the parameter derivative used in the implicit equation is

$$F_\mu = \frac{s_1}{r_1^2} + \frac{2(1-\mu)}{r_1^3} - \frac{s_2}{r_2^2} + \frac{2\mu}{r_2^3}. \tag{18}$$

The manuscript's formula for $dC_i/d\mu$ follows by differentiating C along an equilibrium and using $\Omega_x=0$. The three gap derivatives are $dC_1/d\mu-dC_2/d\mu$, $dC_2/d\mu-dC_3/d\mu$, and $dC_3/d\mu+1-2\mu$. All have strictly positive interval lower bounds. Hence their global minima and maxima occur at the historical envelope endpoints. Certified fixed-parameter brackets at those endpoints then sharpen the interval-panel gap bounds. This monotonicity step is essential: a scan of sampled parameters would not establish the same uniform assertion.

Table S3 | Conservative uniform bounds from the final certificate. Each interval is strictly inside the displayed outer endpoints.

Quantity	Lower endpoint	Upper endpoint
$C_1 - C_2$	0.00127185	0.00127210
$C_2 - C_3$	0.0365307	0.0365351
$C_3 - C_4$	0.00190647	0.00190684
$dx_1/d\mu$	−23.75336	−23.75024
$dx_2/d\mu$	23.91838	23.92165
$dx_3/d\mu$	−0.41666673	−0.41666631
$27\mu(1-\mu)$	0.02572533	0.025730230

The final certificate uses 100 decimal digits and 256 panels; an independent execution at 70 digits and 128 panels establishes the same strict signs. Across these runs and the fixed input checks, 1170 root boxes and associated derived interval records pass the rational replay. Positive interval widths reflect conservative enclosure and parameter dependence, not failed convergence or physical uncertainty. The full certificate includes every panel, root bracket, endpoint sign, derivative enclosure, gap bound, and coverage assertion. Published concise bounds are rounded outward from these records.

The collinear spectral check evaluates $\Omega yy=1-(1-\mu)/r_1^3-\mu/r_2^3$ on every root box. Its upper bounds are strictly negative on all three branches, while $\Omega xx=F_x>0$. Together with $\Omega xy=0$, this certifies saddle–center spectra uniformly. At the triangular points the Routh expression stays below 0.025730230. These mathematical statements do not depend on the nominal kilometer scale.

The proof is conditional on the CR3BP equations and the arithmetic semantics of Python Decimal and Fraction. It is not a proof-assistant formalization, does not certify a full N-body ephemeris, and does not validate the existence of the separately computed periodic orbit. The use of two independent arithmetic representations helps detect implementation errors, but does not eliminate all possible common conceptual errors. The displayed formulas, complete records, and executable checks are provided to make that assumption boundary inspectable.

Dimensional scale hierarchy

All coordinate differences below mean DE440 minus the identified baseline, using the same fixed nominal length unit $a_0=5.20288700$ au. The IAU definition gives 149597870.7 km per au[9]. The resulting unit, 7.783×10^8 km at four significant figures, comes from the approximate J2000 element fit and is not a DE440 osculating separation[10].

Table S4 | Signed differences toward DE440 from each historical baseline. DU values and ΔC are dimensionless; kilometer differences use the same nominal scale. They are not uncertainties.

Baseline	Point	Δx (DU)	Δx (km)	ΔC
Koon / Wilczak	L1	−4.303e-06	−3.349e+03	+4.708e-06
Koon / Wilczak	L2	+4.333e-06	+3.373e+03	+4.466e-06
Efthym.	L1	−1.376e-07	−1.071e+02	+1.505e-07
Efthym.	L2	+1.385e-07	+1.078e+02	+1.428e-07
DE405	L1	+6.752e-10	+5.255e-01	−7.387e-10
DE405	L2	−6.800e-10	−5.292e-01	−7.008e-10
DE431	L1	+1.249e-10	+9.723e-02	−1.367e-10
DE431	L2	−1.258e-10	−9.792e-02	−1.297e-10

The approximate eccentricity e=0.04838624 implies a Keplerian separation-scale variation $\pm a_0 e \approx \pm 3.766 \times 10^7$ km. Holding μ and the circular L1 fractional distance fixed maps that to $\pm 2.511 \times 10^6$ km. This is a comparison of omitted length scales, not a computed elliptic Lagrange point or a bound on physical trajectory error. JPL's quoted 600000 km nominal distance error concerns its approximate-position formula; it is not a covariance or an uncertainty on a_0. The relevant hierarchy is therefore omitted eccentricity scale, historical model-parameter differences, and much smaller arithmetic implementation differences. It would be misleading to combine these into a single error bar.

Sources and preservation

The archive includes original retrieved DE405 and DE431/DE440 input files and the two JPL source pages. The source manifest records retrieval date, original URL, byte count, and SHA-256 checksum. These files permit exact input reconstruction even if a live web page changes. Their versioned official URLs are retained; a bundled snapshot is not described as a newly deposited permanent public archive. No public repository accession or DOI has been invented.

The literature audit records complete metadata and a claim-specific role for each cited article, including 25 recent primary research papers from 2016–2025. It distinguishes ephemeris provenance, local Trojan dynamics, validated methods, and global circular or elliptic dynamics. Bibliographic verification is not represented as an independent reproduction of all the cited papers. Original scholarly PDFs used for checking are not redistributed in this archive; persistent source links and the relevant numeric input descriptions are provided instead. Official datasets and classical algorithm sources remain because they are the primary authorities for the inputs and methods, not because they replace recent research.

Reproduction and acceptance checks

Run the parameter program with a fresh output directory. It requires Python's standard library only and was executed with Python 3.12.14. The numerical dynamics program has a separate dependency specification and was run with Python 3.9.6, NumPy 1.26.4, SciPy 1.13.1, and Matplotlib 3.9.4. It never consumes approximate output of the interval program to construct the certificate. The release assertions require strictly positive gaps, all root-sign and coverage

checks, all rational containment tests, and the spectral signs; they do not use the previous manuscript's arbitrary residual threshold of 10^{-11}.

The former fsolve comparison is no longer part of the principal result. For clarity, the Powell hybrid method combines Newton-type and scaled-gradient directions within trust-region safeguards[11]. The present dynamic root calculation uses Brent's bracket-preserving interpolation/bisection method[12], while the certificate uses monotone root enclosures and exact sign checks. This separation makes the certified result independent of convergence flags from either general-purpose nonlinear solver.

Supplementary Note S3. Dynamical validation and figure specifications

S3.1 Scope, conventions, and reproducibility

This note supplies the full numerical design behind the periodic-orbit, frequency, orientation, and plotting checks. Every quantity is dimensionless unless specified otherwise: DU is the unit primary separation and TU is the reciprocal primary angular speed. The adopted mass parameter is the DE440 Sun–Jovian-system ratio. We retain the unshifted convention

$$C = 2\Omega - v_x^2 - v_y^2, \Omega = \frac{x^2+y^2}{2} + \frac{1-\mu}{r_1} + \frac{\mu}{r_2}. \quad (19)$$

The standalone program `dynamics_validation.py` uses Python 3.9.6, NumPy 1.26.4, SciPy 1.13.1, and Matplotlib 3.9.4 in the recorded execution. Its outputs include the full-precision initial conditions, numerical tables, representative trajectory samples, all figure parameters, eight validation checks, and file hashes. Execute the program with `--output-root` set to the intended output directory; it writes into that directory's `results` and `figures` subdirectories. The source hash and complete numerical environment appear in `dynamics_summary.json`.

The calculations in this note are numerical cross-checks. They do not provide interval enclosures of entire trajectories, prove existence of the approximate periodic orbit, or establish nonlinear stability independently. The certificate in Note S2 has a different scope and uses different arithmetic. Binary64 residuals near machine precision, especially implicit-integrator step counts and small differences of monodromy entries, can vary between software and hardware configurations. Tolerances, conservative bounds, and cross-method agreement are therefore more meaningful than exact equality of the last recorded digits.

Figure S1 supplies a potential-map overview and resolves the two Jovian critical curves. Section S3.5 states its exact grids and masking bounds.

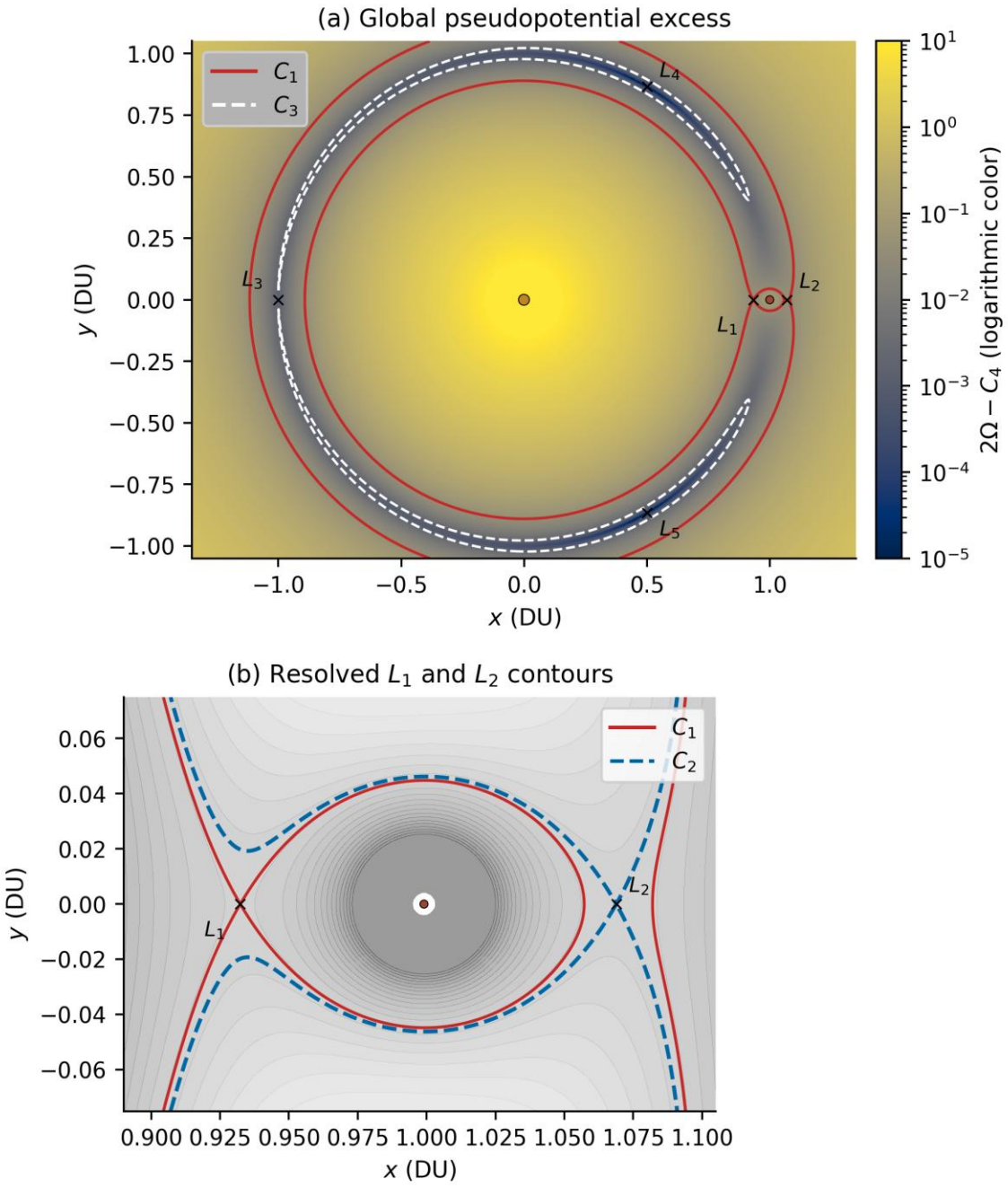


Figure S1 | Pseudopotential excess and resolved Jovian critical curves. (a) Logarithmic color displays $2\Omega - C_4$ on the global grid, with display limits 10^{-5} and 10. The C1 contour is red and C3 is dashed white. (b) The zoom resolves the distinct C1 (solid red) and C2 (dashed blue) curves near L1 and L2. C2 is deliberately omitted from the global overlay. Primary locations and equilibria are marked; coordinate axes have equal aspect. The excluded primary disks and grid sizes are specified in Section S3.5.

S3.2 Differential correction at L1

Write the state as $z = (x, y, v_x, v_y)$. The collinear L1 root for this experiment is calculated independently with bracketed Brent iteration, with absolute root tolerance 5×10^{-15} and relative

tolerance 10^{-14}. The root brackets exclude a 10^{-9} neighborhood of each primary. This binary64 root is used only to initialize the dynamics; the parameter-uniform certificate remains independent.

Fix $x_0 = x_1 - 0.001$, $y_0 = v_{x0} = 0$, and correct the positive initial v_{y0}. The displacement is small compared with the distance between L1 and the secondary. If ω_1 is the positive center frequency of the L1 linearization, the center-mode initial guess is

$$v_{y0}^{(0)} = \frac{\omega_1^2 + \Omega_{xx}(L_1)}{2}(0.001). \tag{20}$$

The program integrates the state together with the state transition matrix Φ:

$$\frac{d\Phi}{dt} = A(z(t))\Phi, \Phi(0) = I_4, A = \frac{\partial f}{\partial z}. \tag{21}$$

The event is the first descending crossing of $y = 0$, excluding the initial ascending departure. Let its time be t_h. The shooting residual is $v_x(t_h)$. With one-based row and column indices, differentiating the event condition gives

$$\frac{dv_x(t_h)}{dv_{y0}} = \Phi_{34}(t_h) - \frac{a_x(t_h)}{v_y(t_h)}\Phi_{24}(t_h). \tag{22}$$

Newton correction subtracts the residual divided by this derivative from v_{y0}. The event integration uses DOP853 with relative tolerance 3×10^{-14}, absolute tolerance 3×10^{-16}, and maximum step 0.025 TU. The first crossing must occur before 8 TU. Iteration stops when the absolute residual is below 2×10^{-14}, with a limit of 15 iterations. Five iterations suffice; the residual decreases from approximately -1.39×10^{-3} to 3.36×10^{-15}. Reversing symmetry yields the full period $T = 2t_h$.

Table S5 summarizes corrected L1 orbit benchmark and measured diagnostics.

Table S5 | Corrected L1 orbit benchmark and measured diagnostics.

Quantity	**Computed value**
Initial x	0.9313654497309743
Initial y and vx	0 and 0
Initial vy	0.007428333222102969
Full period, TU	2.885994032640105
Unshifted C	3.0387156070327146
Full-period reference state closure	1.52×10^{-13}
Maximum sampled reference Jacobi drift	8.88×10^{-16}
Maximum Radau/reference state difference	less than 4×10^{-12}

The printed digits define a reproducibility benchmark, not the physical accuracy of a Sun–Jupiter orbit. Full-precision values in `dynamics_lyapunov_validation.csv` should be used to reproduce the closure test. The reference integration uses DOP853 with tolerances $(3 \times 10^{-14}, 3 \times 10^{-16})$, maximum step 0.0125 TU, and 4001 uniform audit samples on $[0, T]$. Its 232 accepted steps should not be confused with the number of audit samples.

Table S6 summarizes integration settings for the periodic-orbit cross-method comparison.

Table S6 | Integration settings for the periodic-orbit cross-method comparison.

Method	Relative tolerance	Absolute tolerance	Maximum step, TU
DOP853	10^{-10}	10^{-12}	0.1
DOP853	10^{-12}	10^{-14}	0.05
DOP853	3×10^{-14}	3×10^{-16}	0.025
DOP853 reference	3×10^{-14}	3×10^{-16}	0.0125
Radau independent method	3×10^{-13}	3×10^{-15}	0.025

The reported closure is $\|z(T) - z(0)\|_2$; trajectory comparisons take the maximum of the Euclidean state difference over the common 4001-time audit grid. All components use the fixed nondimensional normalization above. This comparison is a refinement and consistency test, not an estimate of an observed convergence order.

Monodromy and conditioning

The full-period state transition matrix is the monodromy matrix M. Its hyperbolic multipliers are approximately 2283.765254 and 0.000437873375. The reference reciprocal-product discrepancy is 4.63×10^{-10}. The other pair is numerically $1 \pm 5.66 \times 10^{-8} i$, consistent with the double unit multiplier of an autonomous Hamiltonian periodic orbit. The small apparent split must not be interpreted as a physical departure from the unit pair.

A symplecticity test requires canonical coordinates. With $p_x = v_x - y$, $p_y = v_y + x$, write $w = Pz$ and $M_c = PMP^{-1}$, where

$$P(x, y, v_x, v_y) = (x, y, v_x - y, v_y + x), \tag{23}$$

$$J_c(a, b, c, d) = (c, d, -a, -b). \tag{24}$$

The absolute Frobenius residual $\|M_c^{\mathrm{T}} J_c M_c - J_c\|_F$ is approximately 1.41×10^{-9} for the reference. Its two-norm condition number is approximately 1.81×10^{7}, and its Frobenius norm is about 4258. The relative residual obtained by dividing the absolute residual by $\|M_c\|_F^2 \|J_c\|_F$ is approximately 3.88×10^{-17}. This scaled value describes the cancellation scale, not an assertion of accuracy beyond binary64 precision. The large hyperbolic multiplier amplifies cancellation in absolute matrix identities. These diagnostics explain why excellent state closure does not justify interpreting every digit of the smaller multipliers.

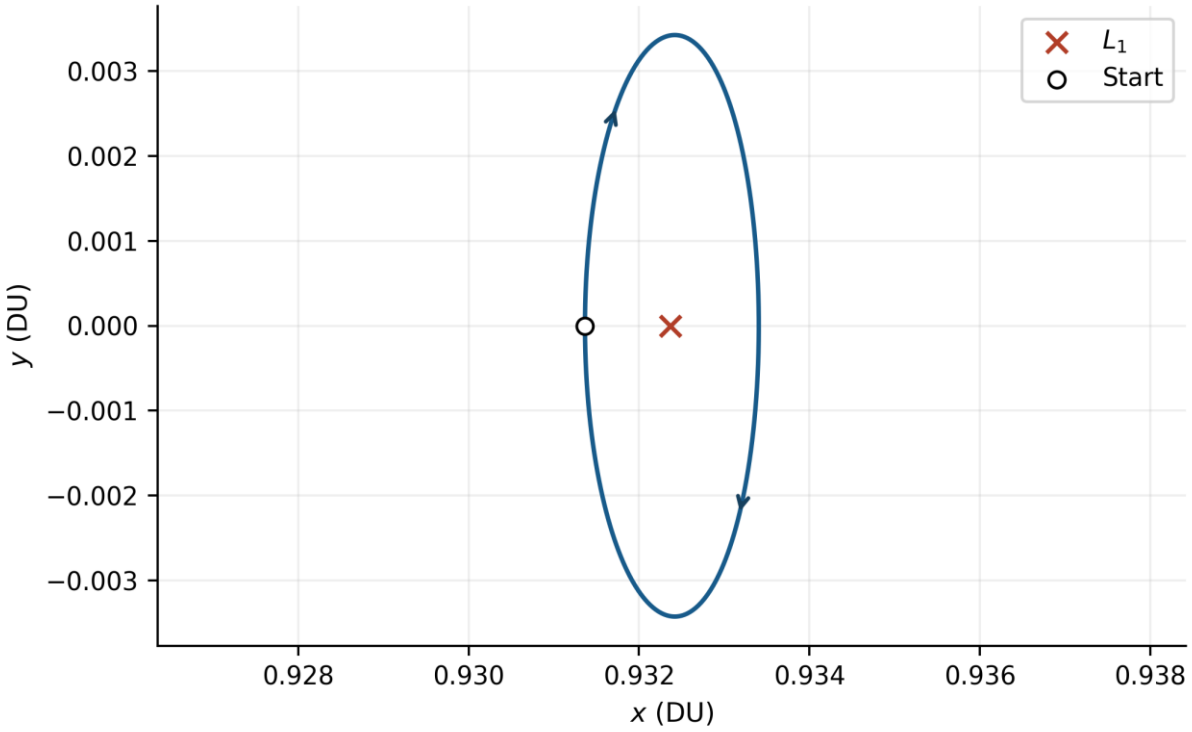


Figure S2 | Corrected planar L1 Lyapunov orbit. The initial displacement is 0.001 DU toward the primary from L1. The start, equilibrium, and direction of motion are marked; the coordinate axes have equal aspect. The period is 2.88599403 TU and C is 3.038715607. The reference trajectory closes within 1.52×10^{-13} in state norm, with independent Radau agreement below 4×10^{-12}. This is a numerical orbit benchmark, not an interval existence proof.

S3.3 L4 trajectories and two-frequency estimation

For each $\epsilon \in \{10^{-5}, 10^{-4}, 10^{-3}\}$, the initial condition is

$$z(0) = (x_4 + \epsilon, y_4, 0, 0). \tag{25}$$

The maximum trajectory displacement is not equal to this initial x offset. The measured maximum distances from L4 over the window are approximately 0.0004078, 0.0040840, and 0.04143 DU, respectively. Each trajectory runs for 800 TU, corresponding to 10.2450 analytical slow cycles and 126.9111 fast cycles. DOP853 uses relative tolerance 10^{-12}, absolute tolerance 10^{-14}, and maximum step 0.2 TU. A reference repeats each case at 3×10^{-14}, 3×10^{-16}, and 0.1 TU. Dense output supplies 40001 uniform samples, with spacing 0.02 TU, for the state and invariant comparisons.

The analytic frequencies and periods are

$$\omega_s = 0.0804641214931, \omega_f = 0.996757505692. \tag{26}$$

$$T_s = 78.0867943449, T_f = 6.30362477463. \tag{27}$$

The frequency estimator uses simultaneous harmonic fitting. If V contains right eigenvectors of the L4 matrix, its modal coordinates are $c(t) = V^{-1}(z(t) - z_4)$. The positive-imaginary slow and fast coordinates are each divided by their root-mean-square amplitude. Their real and imaginary parts form four response series. With the library's unit-norm eigenvectors, the two-norm condition number of V is approximately 102.14. The fitted harmonic design matrix has

condition number approximately 1.433; the final two-column nonlinear fitting Jacobian has condition number between 1.000 and 1.761 across the three cases. These quantities describe numerical conditioning, not probabilistic error bars.

For trial fundamental frequencies (ν_s, ν_f), fit a constant and sine/cosine pairs at

$$k_s\nu_s + k_f\nu_f, 0 < |k_s| + |k_f| \leq 3. \tag{28}$$

Only one representative of each positive/negative pair is retained: $k_s > 0$, or $k_s = 0$ and $k_f > 0$. There are 12 frequency combinations and 25 linear columns including the constant. Linear least squares determines their coefficients at each trial pair; bounded nonlinear least squares minimizes the resulting residual over the two fundamental frequencies. This variable projection uses 4001 samples at spacing 0.2 TU for the complete window. Initial frequencies are the analytical values; each has search bounds of plus or minus 0.003 TU^{-1}. The nonlinear tolerances for parameter and objective changes are 10^{-12}, the gradient tolerance is 10^{-11}, and the relative finite-difference step is 10^{-6}. A limit of 60 nonlinear function evaluations is imposed. All fits satisfy the stopping criteria.

Table S7 summarizes two-frequency estimates at three initial displacements. All frequencies are in inverse normalized time units.

Table S7 | Two-frequency estimates at three initial displacements. All frequencies are in inverse normalized time units.

ε	Slow frequency	Slow relative difference	Fast frequency	Fast relative difference
10^{-5}	0.0804641194030	-2.60×10^{-8}	0.996757505400	-2.93×10^{-10}
10^{-4}	0.0804639125197	-2.60×10^{-6}	0.996757476618	-2.92×10^{-8}
10^{-3}	0.0804431467740	-2.61×10^{-4}	0.996754588225	-2.93×10^{-6}

Relative differences use the corresponding analytical linear frequency in the denominator. Their approximately hundredfold change per tenfold change of initial offset is an observed small-amplitude scaling over these three cases, not a universal law. The fits are not raw Fourier-bin maxima. In particular, the unwrapped argument of an individual linear modal coordinate can give an incorrect winding rate at finite amplitude because other harmonics mix into that coordinate. Raw phase estimates are retained in the data for transparency but are not reported as the measured fundamental frequencies.

The maximum reference-versus-production frequency difference is below 1.4×10^{-12} TU^{-1}, and the maximum sampled state difference is below 9.5×10^{-13}. Increasing the harmonic order from three to four changes the largest-amplitude frequencies by 1.66×10^{-10} and 3.18×10^{-9} TU^{-1}. Fits on the first and second 400-TU halves differ by up to 3.01×10^{-8} for the slow mode and 2.69×10^{-9} for the fast mode at the largest amplitude. Thus fitting-window and truncation effects exceed integration-refinement effects in that case. These are deterministic sensitivity measurements, not statistical confidence intervals.

The normalized harmonic residual is the root mean square over the four normalized response series. At order three it is approximately 3.47×10^{-10}, 1.02×10^{-7}, and 7.71×10^{-5} as the initial offset increases. At order four the corresponding residuals are 3.31×10^{-10}, $2.07 \times$

10^{-10}, and 1.53×10^{-6}. The full residual, window, conditioning, and tolerance comparisons are supplied in the frequency tables.

The maximum sampled Jacobi drift is 8.88×10^{-16}, 1.33×10^{-15}, and 8.88×10^{-16}, respectively. Running maxima plateau near the binary64 evaluation floor over this 800-TU window. No secular increase is resolved by this diagnostic, but the finite window cannot establish a bound at arbitrary future times. Figure 2 of the manuscript uses the running maximum rather than absolute-drift spikes at zero crossings; zero initial drift is omitted from the logarithmic axis without adding an artificial floor.

S3.4 Sign-sensitive orientation checks

Fix the stated positive-z rotation convention and let

$$J(u, v) = (-v, u), H = \nabla^2 \Omega(L_4). \tag{29}$$

For either sign $\sigma = \pm 1$, the linear equation $q'' = Hq - 2\sigma Jq'$ has characteristic polynomial

$$\lambda^4 + (4 - trH)\lambda^2 + detH. \tag{30}$$

It depends on the square of the Coriolis coefficient. Simultaneously reversing both Coriolis terms therefore preserves scalar eigenfrequencies and the Jacobi invariant. Matching those frequencies is useful, but cannot fix orientation by itself.

Let R(t) be the positive-z rotation from rotating to inertial coordinates. Independent Newtonian gravity is computed directly from the two instantaneous inertial primary positions. Correct rotating accelerations must satisfy

$$a_I = R(t)[q'' + 2Jq' - q]. \tag{31}$$

Four collision-free test states with nonzero velocities give agreement to at most 4.45×10^{-16}. Reversing both Coriolis terms produces a residual $R(t)4Jq'$, whose norm is $4\|q'\|_2$; the measured norms range from approximately 0.0832 to 0.1544. The complete test states are in `dynamics_coriolis_orientation.csv`.

A trajectory-level comparison provides another check. For initial offset 10^{-5} DU and $0 \leq t \leq 8$ TU, 4001 uniform times compare the nonlinear trajectory with the exact matrix-exponential linear solution for each sign choice. The nonlinear trajectory is integrated with DOP853 at relative tolerance 3×10^{-14}, absolute tolerance 3×10^{-16}, and maximum step 0.01 TU. The correct linear solution differs by at most 2.52×10^{-8} in state norm, whereas the reversed-sign solution differs by 3.96×10^{-4}. This phase and vector-direction test selects the stated rotating-frame convention despite the identical scalar spectra.

S3.5 Exact plotting grids and masking bounds

The global potential and Hill-region grid contains exactly 1601 x 1201 nodes on $[-1.35,1.35] \times [-1.05,1.05]$. The first three Hill-region insets use 801 x 501 nodes on $[0.89,1.10] \times [-0.065,0.065]$. Figure S1's potential zoom uses 1001 x 701 nodes on $[0.89,1.105] \times [-0.075,0.075]$. The grids are uniform, with no extra inserted coordinates. Every panel has equal coordinate aspect. Points within 0.004 DU of either primary are masked to exclude collision singularities.

The six Hill-region levels are $C_1 + 0.004$, $(C_1 + C_2)/2$, $C_2 - 0.002$, $(C_3 + C_4)/2$, C_4, and $C_4 - 0.0005$. The first four sample every regular interval. Insets display the finite-width L1 and L2 openings. At the last two levels the analytic global-minimum result is used: the zero-velocity locus consists of L4 and L5 at equality and is empty below it. Collision points themselves remain

outside the physical domain. The graphics illustrate energetic accessibility, not an orbit's guaranteed transit through a gateway.

Mask independence follows from an elementary bound. For a primary at barycentric distance $|p|$ with mass fraction m, every collision-free point within radius ρ satisfies

$$2\Omega \geq max(|p| - \rho, 0)^2 + \frac{2m}{\rho} + \frac{2(1-m)}{1+\rho}. \quad (32)$$

The first term bounds barycentric squared distance, the second uses the maximum possible distance to the nearby primary, and the third uses the maximum distance to the other primary. For $\rho = 0.002, 0.004, 0.008, 0.016$ DU, this bound exceeds the largest plotted C for both primaries. The smallest positive margin is 0.00948005, at the Jovian mask with radius 0.016 DU. Hence all tested masks remove only allowed points and cannot erase a forbidden neck or island. This bound is independent of raster resolution.

S3.6 Validation criteria and supplied outputs

Eight automatic checks require: reference orbit closure below 10^{-10}; independent Radau/reference state disagreement below 10^{-10}; reference hyperbolic reciprocal-product discrepancy below 10^{-7}; L4 frequency changes under numerical refinement below 10^{-10}; relative small-amplitude frequency disagreement with the analytical limit below 10^{-6}; correctly oriented inertial-force discrepancy below 10^{-12}; reversed-sign discrepancy above 0.01; and strictly positive allowed-side margins for every mask. All eight pass in the supplied run. These are practical regression criteria, not certified error bounds. The state threshold is 10^{-7} of the prescribed Lyapunov displacement and allows room above the platform-dependent roundoff floor; the frequency threshold tests the analytical small-amplitude limit rather than asserting exact linearity at finite amplitude.

The supporting files include correction iterations, Lyapunov validation and sampled states, L4 frequencies and sampled states, reference and harmonic-order comparisons, phase and inertial-orientation checks, grid and masking bounds, the validation checklist, summary, and checksums. Values should be interpreted together with their full settings and residual definitions. Neither a small residual nor agreement across two integrators makes the circular model a precise representation of the actual Solar System.

References

1. Victor Szebehely. *Theory of Orbits: The Restricted Problem of Three Bodies*. Academic Press (1967). https://doi.org/10.1016/B978-0-12-395732-0.X5001-6.
2. Wang Sang Koon, Martin W. Lo, Jerrold E. Marsden, Shane D. Ross. Heteroclinic connections between periodic orbits and resonance transitions in celestial mechanics. Chaos: An Interdisciplinary Journal of Nonlinear Science 10(2), 427-469 (2000). https://doi.org/10.1063/1.166509.
3. Daniel Wilczak, Piotr Zgliczyński. Heteroclinic Connections Between Periodic Orbits in Planar Restricted Circular Three-Body Problem - A Computer Assisted Proof. Communications in Mathematical Physics 234(1), 37-75 (2003). https://doi.org/10.1007/s00220-002-0709-0.
4. Christos Efthymiopoulos. Nekhoroshev stability estimates for different models of the Trojan asteroids. Proceedings of the International Astronomical Union 2004(IAUC197), 195-204 (2004). https://doi.org/10.1017/s1743921304008658.

5. NASA Jet Propulsion Laboratory. DE405 ASCII ephemeris header, header.405, groups 1040 and 1041. Accessed 16 September 2026. https://ssd.jpl.nasa.gov/ftp/eph/planets/ascii/de405/header.405.
6. NASA Jet Propulsion Laboratory. DE431 mass-parameter kernel, gm_de431.tpc, last modification 8 January 2014. Accessed 16 September 2026. https://naif.jpl.nasa.gov/pub/naif/generic_kernels/pck/gm_de431.tpc.
7. NASA Jet Propulsion Laboratory. Astrodynamic parameters, DE440 planetary-system gravitational parameters. https://ssd.jpl.nasa.gov/astro_par.html (accessed 16 September 2026; source snapshot in Supporting Information).
8. NASA Jet Propulsion Laboratory. DE440 mass-parameter kernel, gm_de440.tpc, 14 December 2022. Accessed 16 September 2026. https://naif.jpl.nasa.gov/pub/naif/generic_kernels/pck/gm_de440.tpc.
9. International Astronomical Union. Resolution B2 on the re-definition of the astronomical unit of length. XXVIII General Assembly (2012). https://iauarchive.eso.org/static/resolutions/IAU2012_English.pdf.
10. NASA Jet Propulsion Laboratory. Approximate positions of the planets, 1800–2050 element fit and nominal errors. https://ssd.jpl.nasa.gov/planets/approx_pos.html (accessed 16 September 2026; source snapshot in Supporting Information).
11. M. J. D. Powell. A hybrid method for nonlinear equations. In P. Rabinowitz (ed.), Numerical Methods for Nonlinear Algebraic Equations, pp. 87–114. Gordon and Breach (1970). https://netlib.org/minpack/.
12. R. P. Brent. An algorithm with guaranteed convergence for finding a zero of a function. The Computer Journal 14(4), 422-425 (1971). https://doi.org/10.1093/comjnl/14.4.422.